

# Observation of flat-band and band transition in the synthetic space

Guangzhen Li,<sup>a,†</sup> Luoja Wang,<sup>a,†</sup> Rui Ye,<sup>a</sup> Shijie Liu,<sup>a</sup> Yuanlin Zheng,<sup>a,b</sup> Luqi Yuan<sup>b, a,\*</sup> and Xianfeng Chen<sup>a,b,c,\*</sup>

<sup>a</sup>Shanghai Jiao Tong University, School of Physics and Astronomy, State Key Laboratory of Advanced Optical Communication Systems and Networks, Shanghai, China

<sup>b</sup>Shanghai Research Center for Quantum Sciences, Shanghai, China

<sup>c</sup>Shandong Normal University, Collaborative Innovation Center of Light Manipulation and Applications, Jinan, China

**Abstract.** Constructions of synthetic lattices in modulated ring resonators attract growing attention to interesting physics beyond the geometric dimensionality, where complicated connectivities between resonant frequency modes are explored in many theoretical proposals. We implement experimental demonstration of generating a stub lattice along the frequency axis of light, in two coupled ring resonators of different lengths, with the longer one dynamically modulated. Such a synthetic photonic structure intrinsically exhibits the physics of flat band. We show that the time-resolved band structure read-out from the drop-port output of the excited ring is the intensity projection of the band structure onto a specific resonant mode in the synthetic momentum space, where gapped flat band, mode localization effect, and flat-to-nonflat band transition are observed in experiments and verified by simulations. This work provides evidence for constructing a synthetic stub lattice using two different rings, which, hence, makes a solid step toward experimentally constructing complicated lattices in multiple rings associated with synthetic frequency dimensions.

Keywords: synthetic dimensions; ring resonators; dynamic modulation; flat band.

Received Feb. 11, 2022; revised manuscript received Apr. 16, 2022; accepted for publication May 25, 2022; published online Jun. 21, 2022.

© The Authors. Published by SPIE and CLP under a Creative Commons Attribution 4.0 International License. Distribution or reproduction of this work in whole or in part requires full attribution of the original publication, including its DOI.

[DOI: [10.1117/1.AP.4.3.036002](https://doi.org/10.1117/1.AP.4.3.036002)]

## 1 Introduction

Synthetic dimensions in photonics have attracted broad interest in recent years.<sup>1–4</sup> They promise new ways to study fundamental physical phenomena with exotic artificial connectivities<sup>5–9</sup> and manipulate light in various ways,<sup>10–18</sup> pointing toward exploration of higher-dimensional physics, beyond three dimensions.<sup>19–21</sup> Among recent experimental achievements, different degrees of freedom of light, including arrival times of pulses,<sup>10,11</sup> frequencies,<sup>22–24</sup> and modal dimensions,<sup>8</sup> have been used to construct synthetic dimensions. Hence, a variety of novel physics have been demonstrated in synthetic dimensions, such as the photonic topological insulator,<sup>8</sup> the Hall ladder with effective magnetic flux,<sup>25</sup> the trajectory of dynamic band structures,<sup>26</sup> and the

topological funneling with non-Hermitian physics,<sup>27</sup> physical models of which are hard to build in structures with only spatial dimensions.

Among these platforms, the dynamically modulated ring resonator system has manifested as a powerful platform where resonant modes with equally spaced frequencies are coupled by external modulation, and then the synthetic frequency dimension is created.<sup>22,23</sup> The modulation applied by external voltages provides the unique advantages of breaking the constraint of fixed geometric structures after fabrication and thus provides an important possibility of achieving complicated functionalities with great experimental flexibility and reconfigurability.<sup>4</sup> Experimental implementations have been performed in ring resonator systems including fiber loops or on-chip micro-rings,<sup>24–26,28–31</sup> and physical phenomena including band structures measurements,<sup>24,26</sup> spectral Bloch oscillations,<sup>29</sup> and non-Hermitian topology<sup>30,32</sup> have been shown, where one ring or two identical rings have been used. On the other hand,

\*Address all correspondence to Luqi Yuan, [yuanluqi@sjtu.edu.cn](mailto:yuanluqi@sjtu.edu.cn); Xianfeng Chen, [xfchen@sjtu.edu.cn](mailto:xfchen@sjtu.edu.cn).

<sup>†</sup>These authors contributed equally to this work.

theoretical proposals have been explored where formations of photonic lattice with different lengths of rings can enable intriguing studies of rich physics, such as the Haldane model,<sup>7</sup> topological quench dynamics,<sup>33</sup> two-dimensional Lieb lattice,<sup>34</sup> three-dimensional topological insulator,<sup>35</sup> and high-order topologies.<sup>36,37</sup> However, to realize these theoretical proposals requires constructing complicated lattice structures beyond simple lines or square geometries in synthetic space in two or more rings of different lengths. Therefore, as a crucial step further, one desires to first prove the capability of creating a complex lattice in two coupled rings of different lengths in the experiment.

In this work, we experimentally couple two rings of different lengths, where one ring undergoes the dynamic modulation, and construct a photonic stub lattice (also called one-dimensional Lieb lattice)<sup>38–42</sup> associated with synthetic frequency dimension. Such a configuration is not straightforward to construct, compared with lattices in one ring<sup>24,26</sup> or in two identical rings.<sup>32</sup> One intrinsic feature of the stub lattice is the natural existence of the flat (dispersionless) band.<sup>43–49</sup> In our experiments, the time-resolved energy bands from the drop-port output of the excited ring are obtained, corresponding to the projection of the band structures of the stub lattice, which, however, is on the synthetic dimension. Moreover, by exciting the resonant modes through the selected input port of one ring and recording the output transmission from the same ring, we observe the effective localization of the resonant modes near the flat band. Such a flat band in synthetic space can further be modified by adding the long-range couplings in the modulation, which leads to the transition from the flat to nonflat bands. By combining theoretical analysis, we show that coupling two rings at different lengths leads to experimental observations where bands are projected onto superposition modes, which is very different from previous works on flat-band physics. Such a feature is unique in the platform of synthetic dimensions with modulated ring resonators, so our work, therefore, exhibits a crucial step toward constructing more complicated synthetic lattices in multiple rings of different lengths.

## 2 Materials and Methods

We start by illustrating the model of two modulated rings of different lengths, labeled as  $A$  and  $B$  in Fig. 1(a). In the absence of group velocity dispersion, the ring resonator supports a set of modes with equally spaced frequencies. If we set the central resonant frequency at  $\omega_0$ , the  $n$ 'th mode in the ring  $A(B)$  has the frequency  $\omega_{A(B),n} = \omega_0 + n\Omega_{A(B)}$ , where  $\Omega_{A(B)} = 2\pi v_g/L_{A(B)}$  is the free spectral range (FSR) of ring  $A(B)$ , and  $v_g$  is the group velocity. We consider the length of ring  $A$  ( $L_A$ ) twice as long as the length of ring  $B$  ( $L_B$ ), i.e.,  $L_A = 2L_B$ , which gives  $2\Omega_A = \Omega_B \equiv \Omega$ . The electro-optic modulator (EOM) is placed inside ring  $A$  with the modulation frequency  $\Omega_M = \Omega/2$ , the modulation strength  $g$ , and the modulation phase  $\phi$ , which provides the connectivity between adjacent resonant modes in ring  $A$ , while there is no modulator in ring  $B$ , so resonant modes in ring  $B$  remain unconnected. Two resonant modes in two rings at the same frequency can be coupled through a fiber coupler with the coupling strength  $\kappa$  [see Fig. 1(b)]. Therefore, three types of modes exist in the system, defined as  $A_n$ ,  $B_n$ , and  $C_n$ , where  $A_n$  and  $C_n$  are the resonant modes at frequencies  $\omega_n$  and  $\omega_n + \Omega/2$  in ring  $A$ , and  $B_n$  is the resonant mode at frequency  $\omega_n$  in ring  $B$  with  $\omega_n = \omega_0 + n\Omega$ . In particular, modes  $A_n$  and

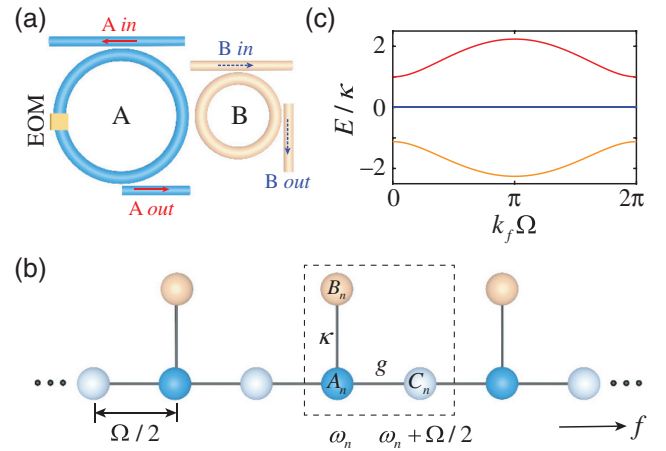


**Fig. 1** Configuration of a synthetic photonic stub lattice. (a) Two coupled ring resonators, where the FSR of ring  $A$  is half of the FSR of ring  $B$ , i.e.,  $2\Omega_A = \Omega_B \equiv \Omega$ . Ring  $A$  undergoes dynamic modulation by placing an EOM with the modulation frequency  $\Omega_M = \Omega/2$ . Waveguides are connected to rings for input/output signals. (b) The system in (a) can be mapped into a photonic stub lattice along the synthetic frequency dimension ( $f$ ), with  $A_n$ ,  $B_n$ , and  $C_n$  indicating three types of lattice sites. (c) The corresponding band structures of the synthetic stub lattice in (b) with  $g = \kappa$  and  $\phi = -0.5\pi$ .

$B_n$  are coupled for the same  $n$ , while  $A_n$  is coupled to  $C_{n-1}$  and  $C_n$  through the modulation under the lowest-order approximation, resulting in the synthetic lattice shown in Fig. 1(b).

The corresponding tight-binding Hamiltonian of the system is<sup>34</sup>

$$H = \sum_n [\omega_n (a_n^\dagger a_n + b_n^\dagger b_n) + (\omega_n + \Omega/2) c_n^\dagger c_n] + \sum_n [\kappa a_n^\dagger b_n + 2g \cos(\Omega t/2 + \phi) (a_n^\dagger c_n + a_n^\dagger c_{n-1}) + h.c.], \quad (1)$$

where  $a_n^\dagger$ ,  $b_n^\dagger$ , and  $c_n^\dagger$  ( $a_n$ ,  $b_n$ , and  $c_n$ ) are the creation (annihilation) operators for the modes  $A_n$ ,  $B_n$ , and  $C_n$ , respectively. Equation (1) can be simplified into the interaction picture by taking the rotating-wave approximation,<sup>50</sup> which results in

$$H_c = \sum_n [\kappa a_n^\dagger b_n + g (a_n^\dagger c_n e^{i\phi} + a_n^\dagger c_{n-1} e^{-i\phi}) + h.c.]. \quad (2)$$

Equation (2) describes the Hamiltonian of a synthetic lattice structure, which is analog to the spatial stub lattice,<sup>38–42</sup> but it is along the frequency axis of light.

To understand the underlying physics of the Hamiltonian described in Eq. (2), we can rewrite Eq. (2) into the  $k_f$  space as follows:

$$H_k = \sum_{k_f} [\kappa a_{k_f}^\dagger b_{k_f} + 2g \cos(k_f \Omega/2 + \phi) a_{k_f}^\dagger c_{k_f} + h.c.], \quad (3)$$

where  $k_f$  is the wave vector reciprocal to the frequency dimension acting as a time variable.<sup>4</sup> The corresponding photonic band structure of the system is then given as

$$\varepsilon_{k_f,0} = 0, \quad \varepsilon_{k_f,\pm} = \pm \sqrt{[2g \cos(k_f \Omega/2 + \phi)]^2 + \kappa^2}, \quad (4)$$

where  $\varepsilon_{k_f,j}$  ( $j = 0, \pm$ ) are the eigenvalues from Eq. (3), corresponding to three bands plotted in Fig. 1(c) within the first Brillouin zone with  $k_f \in [0, 2\pi/\Omega]$ . One can see a flat band  $\varepsilon_{k_f,0}$  in the middle gapped from the upper and lower dispersive bands  $\varepsilon_{k_f,\pm}$ , which indicates that light can be efficiently localized in the flat band without scattering.<sup>44-47</sup> Let  $\psi_{k_f,j} = (\psi_{k_f,j}^A, \psi_{k_f,j}^B, \psi_{k_f,j}^C)^T$  be the eigenstates corresponding to  $\varepsilon_{k_f,j}$ , with  $\psi_{k_f,j}^A$ ,  $\psi_{k_f,j}^B$ , and  $\psi_{k_f,j}^C$  being the projection of the eigenstates on the three modes ( $A_k$ ,  $B_k$ , and  $C_k$ ) in the  $k_f$  space, and then we have

$$\begin{aligned} \psi_{k_f,0} &= (0, -G, \kappa)^T / \sqrt{G^2 + \kappa^2}, \psi_{k_f,\pm} \\ &= (\pm \sqrt{G^2 + \kappa^2}, \kappa, G)^T / \sqrt{2(\kappa^2 + G^2)}, \end{aligned} \quad (5)$$

with  $G = 2g \cos(k_f \Omega/2 + \phi)$ . One notes that the flat band ( $j = 0$ ) has no projection onto mode  $A_k$  due to  $\psi_{k_f,0}^A = 0$ , while the two dispersive bands ( $j = \pm$ ) are antisymmetrically projected onto mode  $A_k$  but symmetrically projected onto modes  $B_k$  and  $C_k$ .

To implement the idea of the synthetic photonic stub lattice described in Eq. (2) for the potential experimental demonstration, we continue with considering a realistic model of two ring resonators coupled with input and output waveguides. In the following, we consider two excitation cases by selectively choosing the input/output ports, which are referred to as  $B$  in  $\rightarrow B$  out and  $A$  in  $\rightarrow A$  out, as in Fig. 1(a). First, we inject the field into the system through the input port of ring  $B$  and measure the drop-port output of ring  $B$  as well ( $B$  in  $\rightarrow B$  out), in which only frequency mode  $B_n$  in ring  $B$  is directly excited. The normalized drop-port transmission  $T_{\text{out}}^B$  can be expressed in the  $k_f$  space as [see Eqs. (S10)–(S14) in the [Supplementary Material](#)]

$$T_{\text{out}}^B(t = k_f; \Delta\omega) = \gamma_B^2 \frac{|\psi_{k_f,j}^B|^4}{(\Delta\omega - \varepsilon_{k_f,j})^2 + \gamma^2}, \quad (6)$$

where  $\gamma_B$  is the coupling strength between ring  $B$  and waveguides,  $\gamma$  is the total loss, and  $\Delta\omega$  is the frequency detuning.  $\varepsilon_{k_f,j}$  and  $\psi_{k_f,j}^B$  are determined by Eqs. (4) and (5), and  $j$  refers to the term having corresponding energy closest to the input frequency. Previous works have demonstrated that the photonic band structure can be measured by time-resolved transmission spectroscopy, where the drop-port output transmission signal is obtained by scanning the frequency of the input laser linearly with time.<sup>24,26</sup> Therefore, Eq. (6) indicates that the band structures read out from the drop-port output of ring  $B$  exhibit the projection of the band structure on mode  $B_k$  in  $k_f$  space.

On the other hand, for the case of  $A$  in  $\rightarrow A$  out, by changing the input/output port to ring  $A$ , similar input/output coupled amplitude equations can be obtained. The corresponding normalized drop-port transmissions in the  $k_f$  space are [see Eqs. (S1)–(S9) in the [Supplementary Material](#)]

$$T_{\text{out}}^A(t = k_f; \Delta\omega) = \gamma_A^2 \frac{|\psi_{k_f,j}^A|^2 |\psi_{k_f,j}^A + \psi_{k_f,j}^C|^2}{(\Delta\omega - \varepsilon_{k_f,j})^2 + \gamma^2}, \quad (7)$$

$$T_{\text{out}}^A(t = k_f; \Delta\omega + \Omega/2) = \gamma_A^2 \frac{|\psi_{k_f,j}^C|^2 |\psi_{k_f,j}^A + \psi_{k_f,j}^C|^2}{(\Delta\omega - \varepsilon_{k_f,j})^2 + \gamma^2}, \quad (8)$$

where  $\gamma_A$  is the waveguide resonator coupling strength of ring  $A$ . Equations (7) and (8) refer to the situation of an input field near resonance with the reference frequencies  $\omega_0$  and  $\omega_0 + \Omega/2$ , respectively. This means that the band structure resolved from the drop-port transmission through ring  $A$  is the projection of the band structure on the superposition modes of  $A_k$  and  $C_k$  separated by  $\Omega/2$  along the frequency dimension.

In experiments, we use two fiber ring resonators coupled together through a  $2 \times 2$  fiber coupler with coupler ratio 70:30, as shown in Fig. S1 in the [Supplementary Material](#). The two rings are excited separately by selectively choosing ring  $A$  or  $B$  as the input port of the laser source ( $A$  in or  $B$  in), while the transmission is recorded from the corresponding drop port ( $A$  out or  $B$  out). After calibration, the lengths of the two rings are  $L_A = 20.4$  m and  $L_B = 10.2$  m, corresponding to  $\Omega_A = 2\pi \cdot 10$  MHz and  $\Omega_B = 2\pi \cdot 20$  MHz. To form the synthetic stub lattice described in Fig. 1(b), we drive the EOM in ring  $A$  by a sinusoidal radio frequency (RF) signal in the form of  $V_M \cos(\Omega_M t + \phi)$  with  $\Omega_M = 2\pi \cdot 10$  MHz, and  $\phi = -0.5\pi$ .

### 3 Results

To demonstrate the construction of the synthetic photonic stub lattice in the experiment, we perform the band structure measurements by finely sweeping the frequency of the input laser through multiple free-spectral ranges.<sup>26</sup> We first inject the laser source into the input port of ring  $B$  and measure the output transmission spectra from the drop port of ring  $B$  ( $B$  in  $\rightarrow B$  out). Figures 2(a3)–2(d3) plot the measured output transmission signals, while each transmission spectrum contains multiple sinusoidal signals, as enlarged in Fig. S2(d) in the [Supplementary Material](#). By breaking the transmission signals into time slices with the time window equaling one roundtrip time of ring  $B$  ( $2\pi/\Omega$ ), i.e., the periodicity of the synthetic stub lattice, one gets the time-resolved band structures, as shown in Figs. 2(a1)–2(d1), with varied modulation amplitude  $V_M$ . We calculate the intensity projections of the band structure on mode  $B_k$  using Eq. (6) and show the results in Figs. 2(a2)–2(d2) with  $\gamma = 0.07\Omega$ , where the width of the bands results from the loss term  $\gamma$  added in the coupled mode equations [see Eq. (S10) in the [Supplementary Material](#)]. The vertical slice of the time-resolved band structure at a fixed time ( $k_f$ ) exhibits a Lorentz function for each of the three bands ( $j = 0, \pm$ ), with  $\gamma$  characterizing the width of each band in Eq. (6), as plotted in Fig. S2(c) in the [Supplementary Material](#). Without modulation ( $V_M = 0$ ), coupled rings result in two Lorentzian resonances of the unmodulated rings, which exhibit two resonances with separation  $2\kappa$  due to energy splitting between two coupled resonant modes  $A_n$  and  $B_n$  [see Fig. 2(a3)]. It leads to two straight energy bands with constant intensity distributions in both experiment [see Fig. 2(a1)] and theory [see Fig. 2(a2)]. The feature of the synthetic stub lattice begins to manifest once the modulation is applied, as shown in Figs. 2(b1)–2(d1), where one notices that three bands exist, and the intensity distributions vary with the modulation amplitude. For a small modulation amplitude [see Fig. 2(b1) with  $V_M = 1.5$  V], the energy of the eigenstate mainly focuses on the upper and lower dispersive bands, which transfers to the middle flat band when the modulation strength becomes larger, as shown in Fig. 2(d1) with  $V_M = 2.5$  V. The

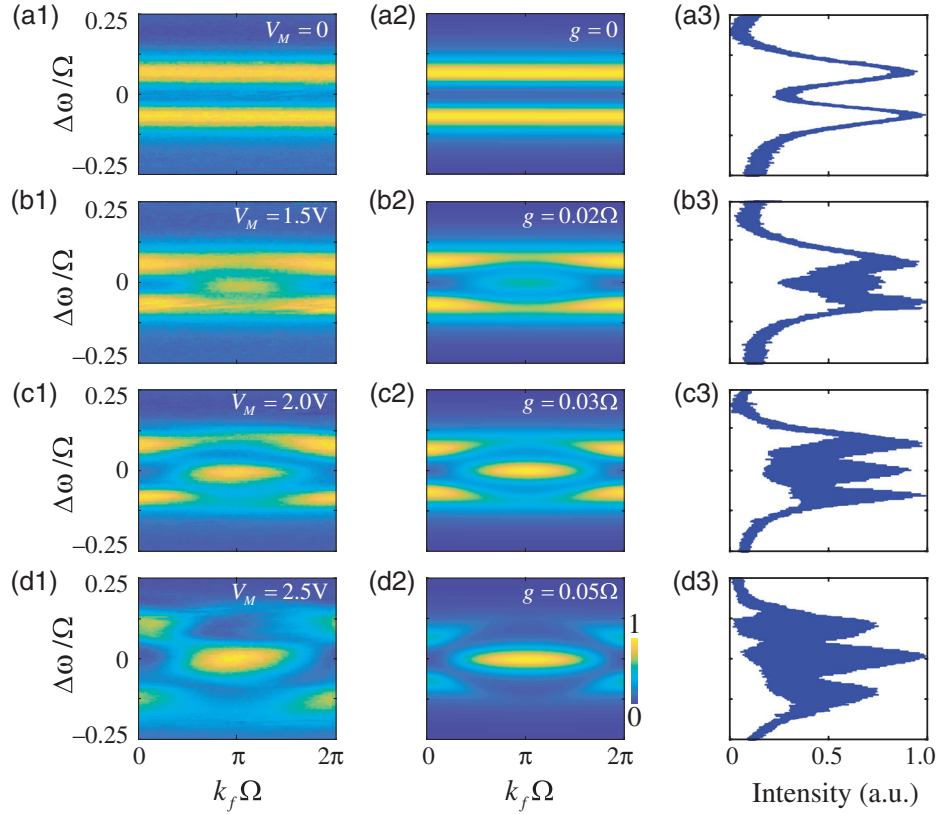


**Fig. 2** Band structure measurements for the case of  $B \text{ in} \rightarrow B \text{ out}$ . (a1)–(d1) Experimentally observed band structures with different modulation amplitudes  $V_M$ . (a2)–(d2) Simulation results of the projected output intensity distribution of the band structure on mode  $B_k$ , based on Eqs. (4)–(6), where  $g$  takes different values with fixed  $\kappa = 0.06\Omega$  and  $\phi = -0.5\pi$ . (a3)–(d3) Measured transmission spectra from the drop port of ring  $B$ . The vertical axis represents the frequency detuning of the input laser source normalized to  $\Omega$ , while the bottom horizontal axis in (a1)–(d2) represents one roundtrip time in ring  $B$  with the period of  $2\pi/\Omega$ .

theoretical plots exhibit excellent agreement with experimental measurements, which clearly shows that the energy of the eigenstate flows from dispersive bands to the flat band when increasing  $g$  [see Figs. 2(b2)–2(d2)]. Moreover, the intensity distributions on the two dispersive bands have a symmetric pattern within the period of  $k_f \in [0, 2\pi/\Omega]$ , which is consistent with the analytical solutions in Eq. (5).

We then consider the case of  $A \text{ in} \rightarrow A \text{ out}$  by switching the input and output fibers to ring  $A$ . The output transmissions of modes  $A_k$  and  $C_k$  separated by  $\Omega/2$  are measured simultaneously, as shown in Figs. 3(a3)–3(c3), where the scale of the vertical axes is twice as large as the scale in Fig. 2. Since in experiments the time window to break the measured output transmission signals of ring  $A$  equals one roundtrip time of ring  $A$  ( $4\pi/\Omega$ ), we measure a combination of intensity projections of the band structure on  $A_k$  and  $C_k$ , which gives  $k_f \in [0, 4\pi/\Omega]$ , as plotted in Figs. 3(a1)–3(c1). Theoretical results from Eqs. (7) and (8) are plotted in Figs. 3(a2)–3(c2) with  $\gamma = 0.07\Omega$ . When there is no modulation, one sees two nearby straight bands near  $\Delta\omega/\Omega = 0.25$  due to energy splitting from coupling between modes  $A_n$  and  $B_n$  and one single straight band near  $\Delta\omega/\Omega = -0.25$ , referring to the resonance of  $C_n$  in both experiment and theory [see Figs. 3(a1) and 3(a2)]. Note that the mode splitting of the top two bands in Figs. 3(a1)–3(a3) is the same as

that in Figs. 2(a1)–2(a3), which is also characterized by  $2\kappa$ . When the modulation is applied, the band structures near  $\Delta\omega/\Omega = \pm 0.25$  show different features. For upper bands near  $\Delta\omega/\Omega = 0.25$ , one sees two dispersive bands, corresponding to the band structure in Fig. 1(c) projected to modes  $A_k$  [see Figs. 3(b1) and 3(c1)], which matches well with the calculated results from Eq. (7) [see Figs. 3(b2) and 3(c2)]. On the other hand, for lower bands near  $\Delta\omega/\Omega = -0.25$ , one can clearly see three bands, with the middle one being flat. The intensity projections of two dispersive bands on mode  $C_k$  are relatively weak in both experiment and theory. Both intensity distributions of the two dispersive bands on modes  $A_k$  and  $C_k$  have the antisymmetric patterns within one period, which matches with the theoretical result in Eq. (5). We shall emphasize that the periodicity of the signal with a time window of  $4\pi/\Omega$  can also be noticed from the superposition term  $|\psi_{k_f,j}^A + \psi_{k_f,j}^C|^2$ , which has unique characteristics from our system where signal amplitudes from modes  $A_n$  and  $C_n$  are mixed in the experiment. Furthermore, the roughness of transmission spectra in both Figs. 2 and 3 originates from the small display of the frequency detuning range for containing multiple sinusoidal signal periods [see Fig. S2(d) in the [Supplementary Material](#)].<sup>26</sup>

Next, we measure the frequency mode distributions for the case of  $B \text{ in} \rightarrow B \text{ out}$  by the heterodyne detection method<sup>51,52</sup> to

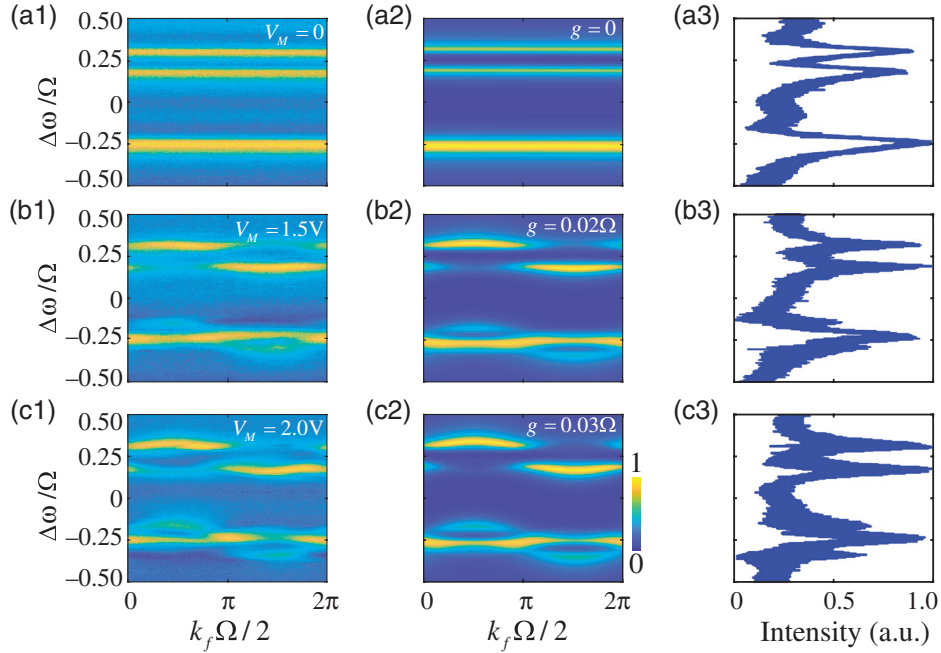


**Fig. 3** Band structure measurements for the case of  $A_{in} \rightarrow A_{out}$ . (a1)–(c1) Experimentally observed band structures varied with  $V_M$ . (a2)–(c2) Simulation results of the projected intensity distribution of the band structure on modes  $A_k$  and  $C_k$ , based on Eqs. (4), (5) and (7), (8), with  $\kappa = 0.06\Omega$  and  $\phi = -0.5\pi$ . (a3)–(c3) Transmission spectra measured from the drop port of ring A. The bottom horizontal axis in (a1)–(c2) represents one roundtrip time in ring A with the period of  $4\pi/\Omega$ .

probe the localization effect of the flat band in the synthetic stub lattice. We connect the acousto-optic modulation path (Fig. S1 in the [Supplementary Material](#)) for frequency shift, and use it to interfere with the drop-port output of ring B by a 50:50 fiber coupler.<sup>53</sup> To show evolutions of frequency modes throughout the whole band structure, we sweep the input laser frequency near the resonance frequency  $\omega_0$  and process the drop-port output transmission through the fast Fourier transform.<sup>54</sup> Figure 4(a) shows the experimentally resolved mode distributions as a function of frequency detuning  $\Delta\omega$ , where the intensities of modes are well confined near  $\Delta\omega \sim 0$ , which refers to the flat band, but spreads over the dispersive bands at  $\Delta\omega \sim \pm 0.07\Omega$ . We explicitly exhibit the mode intensity distributions for two input frequencies in Fig. 4(b), which are  $\Delta\omega = 0$  at the flat band and  $\Delta\omega = 0.08\Omega$  at the upper dispersive band, respectively. For the input frequency at the flat band [see the left part of Fig. 4(b)], one sees that the intensities of modes  $B_n$  mainly locate at the zeroth and  $\pm 1$ st modes with a very small portion diverging to the  $\pm 2$ nd modes. On the other hand, intensities of modes experience spread for the input frequency located at the dispersive band [see the right part of Fig. 4(b)]. Simulations are performed by solving Eq. (6) with sweeping the input frequency and then Fourier transforming the transmitted intensity, in which the loss is chosen as  $\gamma = 0.03\Omega$  for better fitting with the experimental results. One can see a good agreement between experimental measurement in Figs. 4(a) and 4(b) and simulated results in Figs. 4(c) and 4(d), where the slight discrepancy between experiments and simulations originates from the experimental devices and the disturbance of the environment. The stability of the system can be further improved by

utilizing polarization-maintaining fibers and devices or placing the experimental setup in the vacuum chamber.

The existence of the flat band in the constructed synthetic stub lattice is not dependent on the coupling coefficients, i.e.,  $g$  and  $\kappa$  for the weak modulation condition.<sup>39</sup> Further increase of the modulation strength falls on the break of the synthetic stub lattice under the tight-binding limit. In this structure, one can make the band transition between the flat band and nonflat band by simply adding the higher-order modulation to introduce the long-range couplings in the frequency dimension, i.e., with an additional modulation frequency  $\Omega$ , which makes the modulation  $2g \cos(\Omega t/2 + \phi) + 2g' \cos(\Omega t + \phi')$ . The second term in the modulation brings next-nearest-neighbor couplings between two nearby resonant modes  $A_n$  (or  $C_n$ ). In the experiment, we apply the EOM in ring A with the corresponding form of  $V_M \cos(\Omega_M t + \phi) + V_M' \cos(2\Omega_M t + \phi')$ , where  $\Omega_M = 2\pi \cdot 10$  MHz and  $\phi = \phi' = -0.5\pi$ , and perform the measurements in the case of  $B_{in} \rightarrow B_{out}$ , which are shown in Fig. 5. Without higher-order modulation [see Fig. 5(a1) with  $V_M' = 0$ ], the system exhibits the feature of the flat band, which is the same as Figs. 2(c1) and 2(c2). Once the higher-order modulation term is added into the EOM ( $V_M' \neq 0$ ), the middle band gradually turns dispersive, while the upper and lower dispersive bands start to show the nonsymmetrical feature, as shown in Figs. 5(b1)–5(d1). In addition, the gap throughout the entire  $k_f$  space gets closed if  $V_M'$  becomes larger [see Fig. 5(d1)]. We, therefore, show the transition from flat to nonflat bands in Figs. 5(a1)–5(d1), which are in excellent agreement with the simulation results depicted in Figs. 5(a2)–5(d2). The middle band exhibits a dispersive trend once the larger

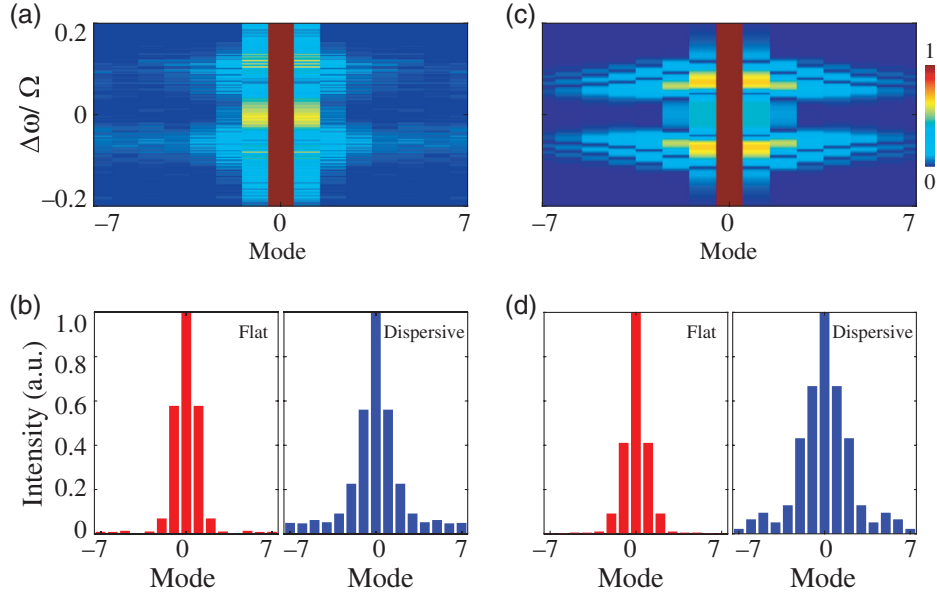


**Fig. 4** Mode distributions for the case of  $B$  in  $\rightarrow$   $B$  out. (a) Experimentally resolved resonant mode spectra as a function of frequency detuning with  $V_M = 3$  V. (b) The corresponding mode distributions of two selected input frequencies in (a) located at  $\Delta\omega = 0$  and  $\Delta\omega = 0.08\Omega$ , respectively. (c) Simulated resonant mode spectra with  $g = \kappa = 0.06\Omega$ , and (d) the corresponding intensity distributions of the two chosen input frequencies at  $\Delta\omega = 0$  and  $\Delta\omega = 0.08\Omega$ , respectively. The horizontal axis represents the mode number  $n$  for the frequency  $\omega_n$ .

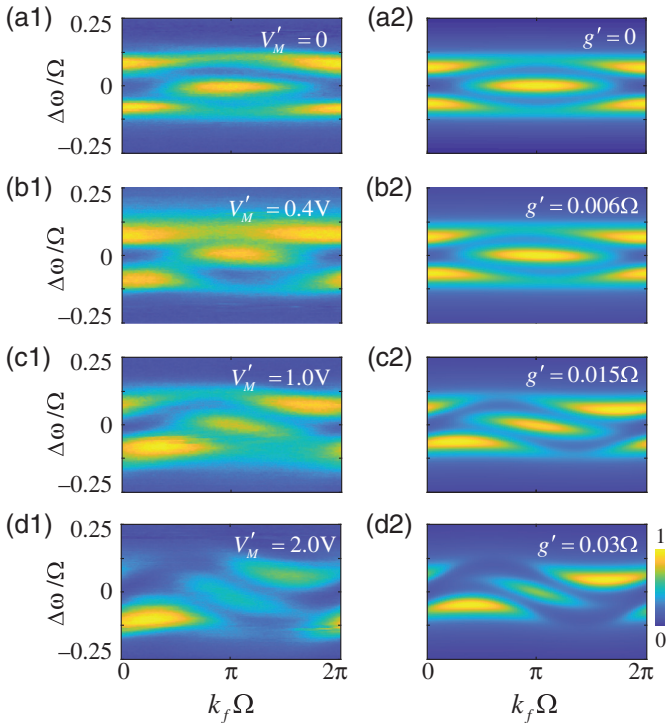


**Fig. 5** Observations of flat-to-nonflat band transition for the case of  $B$  in  $\rightarrow$   $B$  out. (a1)–(d1) Experimentally measured band structures with different long-range modulation amplitudes  $V'_M$  and fixed  $V_M = 2$  V. (a2)–(d2) Simulation results of the projected intensity distribution of the band structure on mode  $B_k$  varied with  $g'$ , where  $g = 0.03\Omega$ ,  $\gamma = 0.07\Omega$ , and  $\phi = \phi' = -0.5\pi$ .

long-range couplings are added, which can lead to the delocalization effect, different from the localization effect observed in Fig. 4. We present this transition between localization and delocalization of light in the frequency dimension with simulation results shown in Fig. S3 in the [Supplementary Material](#). Such an opportunity to dynamically introduce the band transition could be useful for light stopping, which has been proposed in theory.<sup>55,56</sup>

## 4 Conclusion

We have experimentally demonstrated a synthetic photonic stub lattice along the frequency axis of light, constructed by two coupled fiber ring resonators of different lengths. The flat-band feature is observed under two cases by selectively choosing the input and output ports for excitations and transmission measurements, which shows that measured band structures are intensity projections of the band on the different resonant modes in  $k_f$  space. We also observed the localization effect near the flat band with distinctive features from dispersive bands and demonstrated the flat-to-nonflat band transition by adding the long-range couplings in modulations, characterizing the intrinsic physics of the synthetic stub lattice. Theoretical simulations performed agree well with experimental results, showing unique features of synthetic frequency dimensions in measuring signals of superposition modes. The construction of the stub lattice in two coupled rings of different lengths proves the experimental feasibility of connecting multiple rings of different types to construct a complicated lattice beyond the line or square geometry in the synthetic space. Our work also highlights potential toward non-Hermitian/topological<sup>57–62</sup> and quantum photonics<sup>63–66</sup> in coupled modulated ring resonator systems.

## Acknowledgments

We greatly thank Prof. Shanhui Fan for fruitful discussions. The research was supported by National Natural Science Foundation of China (12104297, 12122407, and 11974245), National Key R&D Program of China (2017YFA0303701), Shanghai Municipal Science and Technology Major Project (2019SHZDZX01), Natural Science Foundation of Shanghai (19ZR1475700), and China Postdoctoral Science Foundation (2020M671090). L.Y. acknowledges support from the Program for Professor of Special Appointment (Eastern Scholar) at Shanghai Institutions of Higher Learning. X.C. also acknowledges the support from Shandong Quancheng Scholarship (00242019024).

## References

1. L. Yuan et al., “Synthetic dimension in photonics,” *Optica* **5**(11), 1396–1405 (2018).
2. T. Ozawa and H. M. Price, “Topological quantum matter in synthetic dimensions,” *Nat. Rev. Phys.* **1**(5), 349–357 (2019).
3. E. Lustig and M. Segev, “Topological photonics in synthetic dimensions,” *Adv. Opt. Photonics* **13**(2), 426–461 (2021).
4. L. Yuan, A. Dutt, and S. Fan, “Synthetic frequency dimensions in dynamically modulated ring resonators,” *APL Photonics* **6**(7), 071102 (2021).
5. A. Schwartz and B. Fischer, “Laser mode hyper-combs,” *Opt. Express* **21**(5), 6196–6204 (2013).
6. C. Qin et al., “Spectrum control through discrete frequency diffraction in the presence of photonic gauge potentials,” *Phys. Rev. Lett.* **120**(13), 133901 (2018).
7. L. Yuan et al., “Synthetic space with arbitrary dimensions in a few rings undergoing dynamic modulation,” *Phys. Rev. B* **97**(10), 104105 (2018).
8. E. Lustig et al., “Photonic topological insulator in synthetic dimensions,” *Nature* **567**(7748), 356–360 (2019).
9. K. Wang et al., “Multidimensional synthetic chiral-tube lattices via nonlinear frequency conversion,” *Light Sci. Appl.* **9**(1), 132 (2020).
10. A. Regensburger et al., “Photon propagation in a discrete fiber network: an interplay of coherence and losses,” *Phys. Rev. Lett.* **107**(23), 233902 (2011).
11. A. Regensburger et al., “Parity-time synthetic photonic lattices,” *Nature* **488**(7410), 167–171 (2012).
12. X. Luo et al., “Quantum simulation of 2D topological physics in a 1D array of optical cavities,” *Nat. Commun.* **6**(1), 7704 (2015).
13. B. A. Bell et al., “Spectral photonic lattices with complex long-range coupling,” *Optica* **4**(11), 1433–1436 (2017).
14. T. Ozawa and I. Carusotto, “Synthetic dimensions with magnetic fields and local interactions in photonic lattices,” *Phys. Rev. Lett.* **118**(1), 013601 (2017).
15. C. W. Peterson et al., “Strong nonreciprocity in modulated resonator chains through synthetic electric and magnetic fields,” *Phys. Rev. Lett.* **123**(6), 063901 (2019).
16. L. Yuan et al., “Photonic gauge potential in one cavity with synthetic frequency and orbital angular momentum dimensions,” *Phys. Rev. Lett.* **122**(8), 083903 (2019).
17. D. Cheng et al., “Arbitrary synthetic dimensions via multiboson dynamics on a one-dimensional lattice,” *Phys. Rev. Res.* **3**(3), 033069 (2021).
18. G. Li et al., “Single pulse manipulations in synthetic time-frequency space,” *Laser Photonics Rev.* **16**, 2100340 (2022).
19. D. Jukić and H. Buljan, “Four-dimensional photonic lattices and discrete tesseract solitons,” *Phys. Rev. A* **87**(1), 013814 (2013).
20. I. Petrides, H. M. Price, and O. Zilberberg, “Six-dimensional quantum Hall effect and three-dimensional topological pumps,” *Phys. Rev. B* **98**(12), 125431 (2018).
21. O. Zilberberg et al., “Photonic topological boundary pumping as a probe of 4D quantum Hall physics,” *Nature* **553**(7686), 59–62 (2018).
22. L. Yuan, Y. Shi, and S. Fan, “Photonic gauge potential in a system with a synthetic frequency dimension,” *Opt. Lett.* **41**(4), 741–744 (2016).
23. T. Ozawa et al., “Synthetic dimensions in integrated photonics: from optical isolation to four-dimensional quantum Hall physics,” *Phys. Rev. A* **93**(4), 043827 (2016).
24. A. Dutt et al., “Experimental band structure spectroscopy along a synthetic dimension,” *Nat. Commun.* **10**(1), 3122 (2019).
25. A. Dutt et al., “A single photonic cavity with two independent physical synthetic dimensions,” *Science* **367**(6473), 59–64 (2020).
26. G. Li et al., “Dynamic band structure measurement in the synthetic space,” *Sci. Adv.* **7**(2), eabe4335 (2021).
27. S. Weidemann et al., “Topological funneling of light,” *Science* **368**(6488), 311–314 (2020).
28. Y. Hu et al., “Realization of high-dimensional frequency crystals in electro-optic microcombs,” *Optica* **7**(9), 1189–1194 (2020).
29. H. Chen et al., “Real-time observation of frequency Bloch oscillations with fibre loop modulation,” *Light Sci. Appl.* **10**(1), 48 (2021).
30. K. Wang et al., “Generating arbitrary topological windings of a non-Hermitian band,” *Science* **371**(6535), 1240–1245 (2021).
31. A. Balčytis et al., “Synthetic dimension band structures on a Si CMOS photonic platform,” *Sci. Adv.* **8**(4), eabk0468 (2022).
32. K. Wang et al., “Topological complex-energy braiding of non-hermitian bands,” *Nature* **598**, 59–64 (2021).
33. D. Yu et al., “Topological holographic quench dynamics in a synthetic frequency dimension,” *Light Sci. Appl.* **10**(1), 209 (2021).
34. D. Yu, L. Yuan, and X. Chen, “Isolated photonic flatband with the effective magnetic flux in a synthetic space including the frequency dimension,” *Laser Photonics Rev.* **14**(11), 2000041 (2020).
35. Q. Lin et al., “A three-dimensional photonic topological insulator using a two-dimensional ring resonator lattice with a synthetic frequency dimension,” *Sci. Adv.* **4**(10), eaat2774 (2018).
36. W. Zhang and X. Zhang, “Quadrupole topological phases in the zero-dimensional optical cavity,” *Europhys. Lett.* **131**(2), 24004 (2020).
37. A. Dutt et al., “Higher-order topological insulators in synthetic dimensions,” *Light Sci. Appl.* **9**(1), 131 (2020).
38. M. Hyrkäs, V. Apaja, and M. Manninen, “Many-particle dynamics of bosons and fermions in quasi-one-dimensional flat-band lattices,” *Phys. Rev. A* **87**(2), 023614 (2013).
39. F. Baboux et al., “Bosonic condensation and disorder-induced localization in a flat band,” *Phys. Rev. Lett.* **116**(6), 066402 (2016).
40. S. Rojas-Rojas et al., “Quantum localized states in photonic flat-band lattices,” *Phys. Rev. A* **96**(4), 043803 (2017).
41. B. Real et al., “Flat-band light dynamics in stub photonic lattices,” *Sci. Rep.* **7**(1), 15085 (2017).
42. M. N. Huda, S. Kezilebieke, and P. Liljeroth, “Designer flat bands in quasi-one-dimensional atomic lattices,” *Phys. Rev. Res.* **2**(4), 043426 (2020).
43. R. A. Vicencio et al., “Observation of localized states in Lieb photonic lattices,” *Phys. Rev. Lett.* **114**(24), 245503 (2015).
44. S. Mukherjee et al., “Observation of a localized flat-band state in a photonic Lieb lattice,” *Phys. Rev. Lett.* **114**(24), 245504 (2015).
45. D. Leykam, A. Andreanov, and S. Flach, “Artificial flat band systems: from lattice models to experiments,” *Adv. Phys.: X* **3**(1), 1473052 (2018).
46. S. Xia et al., “Unconventional flatband line states in photonic Lieb lattices,” *Phys. Rev. Lett.* **121**(26), 263902 (2018).
47. J. Ma et al., “Direct observation of flatband loop states arising from nontrivial real-space topology,” *Phys. Rev. Lett.* **124**(18), 183901 (2020).
48. P. Karki and J. Paulose, “Stopping and reversing sound via dynamic dispersion tuning in a phononic metamaterial,” *Phys. Rev. Appl.* **15**(3), 034083 (2021).

49. R. A. V. Pobleto, “Photonic flat band dynamics,” *Adv. Phys. X* **6**(1), 1878057 (2021).
50. M. O. Scully and M. S. Zubairy, *Quantum Optics*, Cambridge University Press (1997).
51. T. Wildi et al., “Photo-acoustic dual-frequency comb spectroscopy,” *Nat. Commun.* **11**(1), 4146 (2020).
52. T. Tetsumoto et al., “Optically referenced 300 GHz millimetre-wave oscillator,” *Nat. Photonics* **15**, 516–522 (2021).
53. “See Supplemental Material for more details on the theory of band structure measurement in two rings and the experimental setup details”.
54. H. J. Nussbaumer, “The fast Fourier transform,” in *Fast Fourier Transform and Convolution Algorithms*, T. S. Huang, Ed., pp. 80–111, Springer (1981).
55. M. F. Yanik and S. Fan, “Stopping light all optically,” *Phys. Rev. Lett.* **92**(8), 083901 (2004).
56. S. Sandhu et al., “Dynamically tuned coupled-resonator delay lines can be nearly dispersion free,” *Opt. Lett.* **31**(13), 1985–1987 (2006).
57. B. Peng et al., “Parity-time-symmetric whispering-gallery microcavities,” *Nat. Phys.* **10**(5), 394–398 (2014).
58. M. Wimmer et al., “Observation of optical solitons in PT-symmetric lattices,” *Nat. Commun.* **6**(1), 7782 (2015).
59. T. Ozawa et al., “Topological photonics,” *Rev. Mod. Phys.* **91**(1), 015006 (2019).
60. Y. Song et al., “Two-dimensional non-Hermitian skin effect in a synthetic photonic lattice,” *Phys. Rev. Appl.* **14**(6), 064076 (2020).
61. Q. Guo et al., “Experimental observation of non-Abelian topological charges and edge states,” *Nature* **594**(7862), 195–200 (2021).
62. Z. Chen and M. Segev, “Highlighting photonics: looking into the next decade,” *eLight* **1**(2), 2 (2021).
63. J. Boutari et al., “Large scale quantum walks by means of optical fiber cavities,” *J. Opt.* **18**(9), 094007 (2016).
64. C. Chen et al., “Observation of topologically protected edge states in a photonic two-dimensional quantum walk,” *Phys. Rev. Lett.* **121**(10), 100502 (2018).
65. H. Chalabi et al., “Synthetic gauge field for two-dimensional time-multiplexed quantum random walks,” *Phys. Rev. Lett.* **123**(15), 150503 (2019).
66. C. Joshi et al., “Frequency-domain quantum interference with correlated photons from an integrated microresonator,” *Phys. Rev. Lett.* **124**(14), 143601 (2020).

**Guangzhen Li** is an assistant researcher in the School of Physics and Astronomy at Shanghai Jiao Tong University (SJTU). She received her PhD in physics from SJTU in 2017 and then worked as a postdoctoral

and assistant researcher in the Laboratory of Advanced Photonic Materials and Physics (LAPMP) at SJTU. Her current research interests are synthetic dimensions in photonics, topological photonics, nonlinear optics, and integrated photonics.

**Luojia Wang** is an assistant researcher in the School of Physics and Astronomy at SJTU. She received her PhD from Peking University in 2013. She worked as a postdoctoral scholar at Texas A&M University, Tongji University, and SJTU, respectively. Her research interest focuses on the theoretical study of quantum optics, nanophotonics, ultrafast nonlinear optics, and topological photonics.

**Rui Ye** is a PhD student in the School of Physics and Astronomy at SJTU. He received his bachelor’s degree from the School of Physical Science and technology at Northwestern Polytechnical University in 2020. His research focuses on synthetic dimensions in photonics, topological photonics, and integrated photonics.

**Shijie Liu** is a postdoctoral researcher in the School of Physics and Astronomy at SJTU. He obtained his PhD in physics from SJTU in 2019 and worked as a postdoctoral researcher in LAPMP at SJTU. His research is focused on the fabrication of integrated photonic devices and nonlinear optics.

**Yuanlin Zheng** is an associate researcher at SJTU’s School of Physics and Astronomy. He obtained his PhD in optics from SJTU in 2013 and subsequently worked as a postdoctoral, assistant, and associate researcher in LAPMP at SJTU. His research focuses on nonlinear optics and integrated photonics for light-matter interaction and light manipulation applications.

**Luqi Yuan** is currently on the faculty in School of Physics and Astronomy at SJTU. He received his PhD in physics from Texas A&M University in 2014 and was a postdoctoral scholar from 2014 to 2018 at Stanford University. His research interests span broad fields among quantum optics, photonics, AMO physics, and nonlinear optics, including nanophotonics, topological photonics, synthetic dimensions in photonics, hybrid quantum systems, and light-matter interactions.

**Xianfeng Chen** is a distinguished professor in School of Physics and Astronomy at SJTU. He obtained his PhD in physics at SJTU in 1999. He is the executive director of the research center for optical science and engineering at SJTU. His current research focuses on advanced photonics materials and devices, nonlinear optics, nanophotonics, quantum optics, and ultrafast optics.